Self-assembly Mechanisms in Plant Cell Wall Components

Yogesh K. Murugesan[1], Damiano Pasini[2] and Alejandro D. Rey[*,1]

[1]*Department of Chemical Engineering, McGill University, 3610 University Street, Montreal, Quebec, H3A 2B2, Canada*
[2]*Department of Mechanical Engineering, McGill University, 817 Sherbrooke West, Montreal, Quebec, H3A 2K6, Canada*

ABSTRACT: This review on self-assembly in biological fibrous composites presents theory and simulation to elucidate the principles and mechanisms that govern the thermodynamics, material science, and rheology of biological anisotropic soft matter that are involved in the growth/self-assembly/material processing of these materials. Plant cell wall, a multi-layered biological fibrous composite, is presented as a model biological system to investigate self-assembly mechanisms in nature's material synthesis. In order to demonstrate the universality of the presented models and the mechanisms investigated, references to other biological/ biomimetic systems are made when applicable. The integration of soft matter physics theories and models with actual biological data for plant cell walls provides a foundation for understanding growth, form, and function in biological material and offers a firm platform for biomimetic innovation.

1 INTRODUCTION

The emerging field of biological material science and engineering (BMSE) has three prominent components: biological (natural) materials, biomaterials (synthetic materials used in bio-environments) and biomimetics or bio-inspired materials, devices, and structures [1]. One of the main driving forces of BMSE is synthesized in the Arzt's pentahedron paradigm [2], which encompasses low temperature/pressure material synthesis in aqueous phases, formation through self-assembly (including directed, equilibrium, and dynamic), optimized multifunctionality (heat and mass transfer, optics, mechanics, electromagnetics), hierarchical multiscale structures, and evolution (Figure 1). The Arzt's pentahedron paradigm has provided a unifying tool to characterize natural material.

A demonstrative example of this efficient material synthesis by a living system in nature is the structural and functional versatility of the muscle mass [3], eye [4] and gladius or pen [5] achieved by squids. At nano- and micro-scales these systems build strong hierarchically structured microfibers made of nanofibrils of proteins and polysaccharides such as collagen [6] and protein [7] coated chitin fibers. These fibers are further strategically aligned through supramolecular self-assembly driven by entropic, chiral interactions between them and anchoring to confining surfaces to form the twisted plywood architecture [8] as observed in squid arms and tentacles [3]. At the tissue level, these structures are further specialized by varying the cell-extracellular matrix organization patterns resulting in materials of diverse material properties and functionalities. Despite being built of the same or similar biochemical precursors, the ultra-structural variations result in structures of diverse functionality: the muscles in the arms of the squid serve in bending and grasping, while the muscles in the tentacle are capable of rapid extension facilitating an efficient prey capture mechanism [3] the eyes of the squid form a highly-distributed Bragg stack that combined with its geometry plays a vital role in camouflaging in their living environment as a protective mechanism against their predators [4]. The gladius or the pen of the squid is a dorsal body wall made of chitin-protein networks that forms as a protective layer that facilitates jet propulsive swimming [5]; we note that similar chitin-protein networks in lobsters form the protective hard shell (the exoskeleton) [9]. Similar multiscale structural optimization has also been observed in cellulose-based systems such as the plant cell walls [10]. Understanding both the optimization of material properties at multiple length scales and the strong integration between these optimized

Corresponding author: alejandro.rey@mcgill.ca
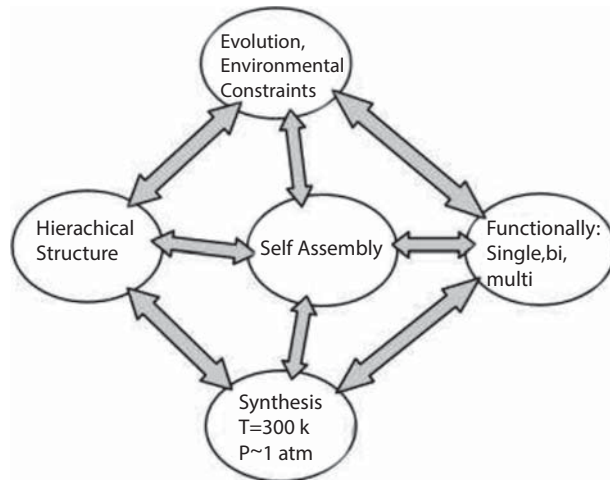
Figure 1 The Arzt's pentahedron paradigm [2]: Schematic representation of unique characteristics that distinguish biological systems from their synthetic counterparts. (Adapted from ref. [2])
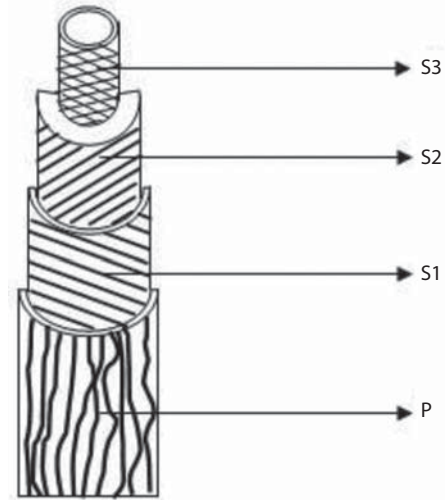
Figure 2 Architecture of multilayered plant cell wall, P – Primary cell wall, S1, S2, S3 – Secondary cell wall layers 1, 2, 3. (Adapted from ref.[16])

structural organizations and the mechanisms that build these efficient structures plays a crucial role in elucidating the principles underlying nature's material synthesis and extending the gained knowledge to several biomimetic material synthesis applications. Design of novel materials with unique properties mimicking biological materials (a) synthesized from inorganic precursors of superior mechanical and thermal properties [11] and (b) synthesized from organic precursors such as chitin/cellulose nanofibers from insect exocuticle/plant cell wall and fibroin inspired by spider silk, following nature's efficient material processing routes have been demonstrated [12,13]. The focus of this review article is liquid crystal self-assembly, nature's energy-efficient material synthesis mechanism that plays a crucial role in building these materials with varied material properties and imprinting multifunctionality into them. The plant cell wall (PCW), nature's most abundant biological fibrous composite, is investigated as a model biological material. In order to demonstrate the universality of self-assembly mechanisms in nature, reference to other biological materials besides PCWs are made where applicable.

1.1 Microstructure of Plant Cell Wall

Plant cells are encompassed by a stiff, multilayered, viscoelastic-viscoplastic composite wall [14] which is rigid enough to function as a supporting structure and at the same time allows surface expansion facilitating cell growth. The typical thickness of plant cell walls

generally varies from 0.1 µm to 0.3 µm [15], about 100 times thinner than the size of the plant cell itself. It is made of sequentially deposited layers of different thickness, chemical composition and structural organization. In Figure 2, the primary cell wall (P) is the first layer to be laid down after cell division and its formation coincides with cell growth. When the cell reaches its final size, three layers of secondary cell wall S1, S2 and S3 are laid over the primary cell wall, in an inward direction. The central layer, called secondary layer 2 (S2), comprises about 80–90% (by the entire cell wall volume). Towards the lumen (a cavity left by the cell after shrinkage and death of the cell) is the secondary layer 3 (S3). At the other side of S2, there are the secondary layer 1 (S1) and the primary cell wall (P) [16]. Growing cells are surrounded by primary cell wall and lack secondary cell wall layers. The primary cell wall has the following functions: it supports the cell membrane against the turgor pressure contained within the cell; it undergoes an enzyme controlled expansion under turgor pressure and regulates the direction of expansion contributing to the growth and the form of a plant; it cooperates with adjacent cells under turgor pressure to build a three-dimensional tissue. The secondary cell walls provide additional mechanical strength to the tissue and in some seeds perform energy storage [16]. The shape of the cell wall depends on the types of cells. For example, compression wood cells of spruce are cylinders of circular or elliptical cross-section, while normal wood cells of spruce are often cylinders with super-elliptical cross-section.

1.2 Plant Cell Wall Components and Organization

The PCW is an excellent example of how nature can use a few widespread natural elements, usually C, H, O, and N, to tailor molecules of diverse structures performing a wide variety of functions [10]. The PCW can be considered as a reinforced biological fiber-laden composite membrane consisting of well-aligned cellulose microfibrils (CMFs) of high tensile strength coated with hemicellulose and embedded in a matrix of polysaccharides (pectin/lignin) and structural glycoproteins [14]. Different plant species are known to synthesize cell walls with a wide range of mechanical properties by varying the arrangement of these building blocks (cellulose, lignin, hemicellulose and pectin) in the cell wall and/or cellular structure [17]. Thus understanding the process through which the CMFs are oriented in a specific direction is crucial to unravelling the mechanisms underlying nature's material synthesis.

Earlier theoretical approaches used to predict the orientation of CMFs in the extra cellular matrix have resulted in a biomechanical model based on open fiber-reinforced cylinder. These approaches have postulated that the fiber orientation angle with respect to the long axis of the cylinder should be 54.7° at maximum volume of the cylinder and that the volume of the cylinder will diminish towards zero at lower and higher fiber angles [18]. However this prediction contradicts experimentally observed microfibril angles in PCWs, where the CMFs are oriented in strategic directions to generate commonly observed textures such as line, helix, ring, crossed helix and helicoid [19] (Figure 3).

1.3 Basic Cell Wall Textures

In the line (ring) mode, the CMFs are aligned parallel (perpendicular) to the major axis of the cell. In the helical mode, the CMFs are oriented obliquely to the major axis of the cell. Table 1 presents XRD measurements
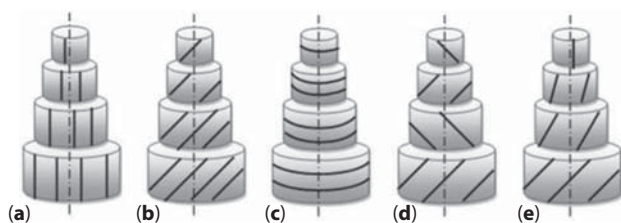
Figure 3 Basic plant cell wall textures: **(a)** line, **(b)** helix, **(c)** ring, **(d)** crossed helix and **(e)** helicoid. The black lines indicate the CMFs and the dashed line represents the major axis of the cell. (Adapted from ref. [19])

of average microfibril angle (CMF orientation with respect to the major axis of the plant cell) in cell walls of some plant species ranging from 0–90° [20].

In expanding cell walls, the line (ring) mode in the primary cell wall promotes radial (axial) expansion of cells and thus plays a major role in anisotropic cell growth. Thus the orientation of CMFs in the primary cell wall controls the shape of the cell and contributes to the morphology at the tissue and organ level. The orientation of CMFs in secondary cell wall layers governs the mechanical properties of wood. The helicoidal structure, also known as the twisted plywood architecture, is the most abundant extracellular structure found in plant cell walls and many other biological fibrous composites found in living systems. The plant cell wall twisted plywood architecture and its variations have been reported in algae, lower plants and higher plants in a variety of tissues such as root hair, petiole, leaf epidermis, hypocotyl, fruit endocarp, and seed epidermal walls [21]. They may occur in both primary and secondary cell walls, although in the primary cell wall they are transient and fragile [22]. This laminated organization is characterized by a series of planes with fibers laid down parallel in each layer and where the direction of the CMFs changes from layer to layer by a regular angle, e.g., 10–20°, as in the stairs of a spiral staircase [21,23]. Schematically, parallel straight lines lying on equidistant planes depict the orientation of fibers in this stratified structure [21–23]. For convenience, only certain equidistant layers are represented in Figure 4(a). One of the most distinctive characteristics of the twisted (helicoidal) plywood architecture is the series of superimposed nested arcs, visible on any cross section oblique to the lamellae (Figure 4(b)).

When observed under polarized light microscopy, the twisted plywood structural design exhibits periodic extinction of light. As an example, Figure 5 depicts a representative electron micrograph of the stone cell of a pear (secondary cell wall) and mung

Table 1 XRD measurement of CMF orientation in cell walls of some plant species [19].

Species	Microfibril angle (ϕ)
Abies sachalinensis	3–14°
Larix kaempferi	9–21°
Picea jezoensis	17–32°
Pinus nigra	25–40°
Picea abies	39° (S2) 89° (S1)
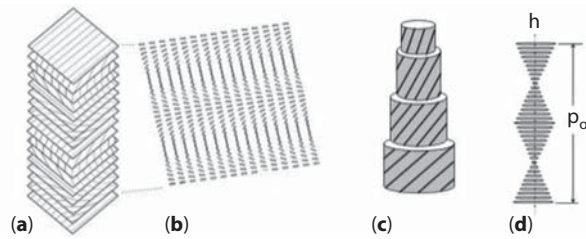
Figure 4 Schematics of the helicoidal plant cell walls. **(a)** The schematic represents parallel and equidistant planes. On each parallel plane, lines indicate the fiber orientation. The fibrillar direction rotates by a small constant angle from one layer to the next, **(b)** Oblique sectional plane showing arced patterns, **(c)** Cylindrical twist architecture. On each coaxial cylinder, parallel and equidistant helices indicate the orientation of the fibers; the angle of helices relative to the axis is constant on each cylinder but rotates slowly from one layer to the other, **(d)** The helix axis 'h' and the helicoidal pitch p_o. (Adapted from ref. [23])
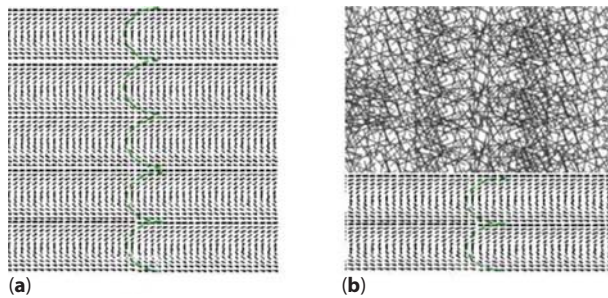
Figure 5 Arced patterns in plant cell walls. (a) Oblique section of secondary cell wall in stone cell of pear showing uniform equidistant nested arcs. (Schematic adapted from de Luca and Rey 2003 as a representative of experimental observations by Roland *et al*. 1987). (b) Oblique section of a primary cell wall in mung bean hypocotyl regions of uniform arced pattern and diffusive wall lacking arced patterns. (Schematic adapted from de Luca and Rey 2003 as a representative of experimental observations by Vian *et al.* 1993)

bean hypocotyl (primary cell wall) in early growing stage exhibiting arced patterns typical of the helicoidal architecture [22,24].

In plant tissues, the twisted plywood organization is also widely detected in the cylindrical geometry due to the cell shape. In this case, the parallel and equidistant planes become a set of coaxial cylinders; the fiber directions being represented by parallel helices. The angle of the helices in a plane relative to the cylinder axis is constant but changes slightly from one cylinder to the next [23]. A schematic representation of helicoidal organization in cylindrical geometry is illustrated in Figure 4(c). The helicoidal plywood is

a unidirectional periodic structure in which the CMF organization pattern repeats over a length $P_0/2$, where P_0 is the helicoidal pitch (few micrometers), and the distance over which the CMF orientation undergoes a 2π rotation, as shown in Figure 4(d). In plant cell walls, the axis of the spiral arrangement 'h' is perpendicular to the cell surface.

In this type of architecture, by having a varied orientation in consecutive layers of the helicoid, the materials attain good mechanical properties in all directions, which increases the fracture strength since the path of any crack will be diverted by the change in orientation, resulting in an increased capacity to dissipate energy. For helicoids, the stiffness efficiency η of the ensemble of fibers can be written through the modified Krenchel equation [21]:

$$\eta = \Sigma \chi \cos^4 \phi / \pi \qquad (1)$$

where χ is layer-to-layer fiber angle, ϕ is the angle between the fiber and the direction of stretching and the summation is over all the layers. It is found that for helicoids η=0.375 regardless of pitch, applied force direction and layer-to-layer angles, thus being equally stiff in all directions normal to the helix direction [21]. The mechanisms by which the microfibrils are oriented in a specific direction are not well understood [19].

1.4   Hypotheses for Cell Wall Texture Formation

The major hypotheses on CMF alignment in plant cell walls are: (a) a theory widely recognized among plant scientist is based on the microtubule-microfibril paradigm [21]. This model assumes that the cortical microtubules are aligned in a well-ordered array inside the plant cell and this spatial information is transformed to the cellulose-synthesizing machinery on the plasma membrane of a growing plant cell that in turn results in the ordered deposition of CMFs in plant cell walls [25]. However, several studies on growing plant cells demonstrate that drug-induced microtubule disassembly does not abolish the oriented deposition of CMFs [26]. Also it is known that in fully expanded cells, cortical microtubules and the most recently deposited CMFs are not generally aligned in the same direction [27]. From these observations, it is evident that microtubule order induced alignment of CMF alone cannot explain the CMF orientation in plant cell walls; (b) an alternative theory, the membrane flow hypothesis assumes the cellulose synthase complexes on the plasma membrane are in motion driven by synthesis and crystallization forces

of CMF [28]. Though there is experimental evidence confirming the mobility of cellulose synthase complexes on the plasma membrane, the assumption that the protoplast rotates relative to the cell wall is actively disputed as this rotation has not been observed in plants [27]. In addition, a purely geometric model also based on cell geometry, inter-fibril distance within a cell wall lamellae and the density of active cellulose synthase complexes has been proposed [27]. Despite this model's ability to predict all the five ideal cell wall textures shown in Figure 3, it cannot explain the deviations from ideal helicoidal texture such as defect textures observed in the presence of secondary inclusions in some plant cell walls. The important parameter of the model, movement pattern and activation rate of cellulose synthase complexes has also not yet been validated experimentally [27]; (c) another well-reasoned hypothesis is that the liquid crystalline (LC) self-assembly model that is based on the structural similarities between the helicoidal cell wall texture and cholesteric LC phases. This model incorporates the fact that the helicoidal texture arises through LC self-assembly that occurs at sufficiently high concentration of the CMFs, when the excluded volume of the CMFs is minimized in the presence of chiral interactions. A review supporting this hypothesis, based on anatomy and developmental biology processes, has emphasized the necessity of characterizing the nature of the forces inducing this self-assembly [29]. Supramolecular self-assembly of biological LC polymers resulting in materials/phases with self-organized structures have been reported in all kingdoms of life. Table 2 shows a compilation of biological systems that exhibit ordered LC mesophases. The observed mesophases in biological systems can be classified into [30,31]: (i) LC analogues (left column), where the LC type of packing is observed frozen-in in the solid state; (ii) mesophases observed in the native state of the biopolymer (middle column), and (iii) LC phases observed in biopolymer solutions in a controlled environment (right column).

The varied biochemical groups and biological origin of the mesogens presented in Table 2 shows that LC order is ubiquitous in the development of functional and structural biological materials. However, this hypothesis for the development of helicoidal plywoods in plant cell wall has been contested on the grounds that there is not enough material to form a LC phase during development of helicoidal plywoods in plant cell walls. Due to the lack of *in vivo* experimental evidence, the nature of the phase operating during cell wall morphogenesis, the amount of cell wall material present and the effective diameter of the microfibrils due to surface charges are not yet characterized. There appears to be no clear consensuses among plant cell wall researchers from various backgrounds on the validity the above theories owing to the lack of experimental techniques verifying their assumptions. In the absence of experimental techniques, theory and simulation can be used as a pragmatic tool that may resolve time and length scales not easily accessible to experiments. Hence the focus of this review is on the formation of plant cell wall microstructure through LC self-assembly. A brief introduction to LC materials and some known applications of theoretical models based on the physics of these materials to biological systems are presented.

Table 2 Compilation of self-assembling biological LC materials and LC analogues observed in nature. (Adapted from ref. [31])

Biological Analogues	*In vivo* Solutions	*In vitro* Solutions
Plant cell walls [21]	DNA [36]	Collagen [35]
Connective tissues in mammals and cephalopods [5,21]	Chromosomes of dinoflagellate and bacteria [37]	Cellulose [35,43]
Dermal scutes and scales of fish [33]	Collagen in egg shell and glands of dogfish [38]	Chitin [35]
		DNA [35]
		Viral suspensions [44]
Exoskeleton of insects and crustaceans [21]	Oothecal gland protein of *S. tenuidentata* [39]	Actin [45,32]
Membranes of animal eggs [21]	Spider silk [40]	
		Flagella of *Salmonella typhimurium* [45,32]
Skin of Mandrill [34]	Sickle cell hemoglobin [41]	Mucin [46]
Human compact bones [35]	Synovial fluid [42]	PBLG [36]
Squid muscle mass [8]		Xanthan [36]
		Quince seed mucilage [21]

1.5 Liquid Crystals – The Fourth State of Matter

Liquid crystallinity (LC) is a state of matter that has molecular ordering between that of stable solids and mobile fluids and hence it is called "mesophase." As the result of this intermediate molecular ordering, these states possess a liquid-like fluidity and solid-like anisotropic molecular order [30]. Molecular ordering in a system can be defined in terms of a) Positional order that refers to the extent to which a group of molecules shows translational symmetry and b) Orientational order that represents a measure of the tendency of the molecules to align along the director on a long-range spatial scale. Molecules in solids possess both positional and orientational order, while those of liquid lack both these long-range orders. LCs have long-range orientational order and can have partial or no positional order.

1.6 Classification of LCs

Depending on the behavior of LCs with respect to physical variables, they are classified as thermotropic LCs and lyotropic LCs. Transitions involving thermotropic LCs are effected primarily by change in temperature and secondarily by pressure. In this type of LC, every molecule participates equally in long-range ordering and the transition from unordered (isotropic) to ordered state (mesophase) is driven mainly by van der Waals interactions. These molecules are of interest in applications such as electro-optic displays, temperature and pressure sensors. In lyotropic LC phases, the transitions are effected primarily by change in concentration of the molecules and secondarily by change in temperature. The phase transition in this class of LCs is due to excluded volume repulsive forces. This category of LCs is important in the context of the current work as they play a major role in living systems.

The simplest LC phase is the nematic mesophase, which is characterized by a long-range orientational order (the long axes of the molecules tend to align parallel to each other along a preferred direction) and lack of positional order (there is no long-range correlation of the positions of molecular center). This preferred average molecular direction is called "director," represented by the unit vector **n**. Defining a director at every spatial "point" of the LC sample (**n**(x,y,z)) leads to a macroscopic description of the preferred average molecular orientation in the material.

When the molecules are intrinsically chiral, i.e., molecules without mirror symmetry such as cellulose, or possess a chiral charge distribution, or when a chiral dopant is added to nematic LC phases, the nematic phase undergoes helical distortion resulting in the cholesteric or chiral nematic LC phase. Cholesteric LC is a helicoidally layered stack that behaves like a nematic at short scales, i.e., in each infinitesimal layer of this three-dimensional assembly, the molecules have a uniform orientation. However, from one layer to the next, their orientation changes by a slight constant angle, leading to a periodic layered configuration characterized by a length scale known as the pitch p. The pitch is defined as the distance required along the helical axis, i.e., axis normal to the successive layers, for the cholesterogens (molecules forming cholesteric structure) to accomplish a rotation of 2π radians. Figure 4(a) depicts the structure of a cholesteric LC order. When the cholesteric pitch tends to infinity, the phase becomes weakly chiral and has characteristics of nematic mesophase. The pitch of the cholesteric LC is usually measured in microns and is affected by physicochemical factors and applied external fields. In lyotropic LCs, the pitch is a function of flexibility/charge/concentration of molecules making up the mesophase, pH, osmotic pressures and stress/electric/magnetic fields. Chiral self-assembly of plant cell wall components and other biological materials resulting in LC analogues that are structurally similar to cholesteric LCs is the central theme of this review.

Liquid crystals are ordered phases responsive to surface constraints and external fields that can cause localized elastic deformations in the molecular field. This property often leads to local symmetry breaking in these phases, resulting in a rich and complex variety of topological defects in the form of points, lines and walls. The types of defects are unique to the types of mesophases, and hence they are the identifying features of the LC phases. Some of the defects in cholesteric mesophases observed in plant cell systems are presented in Section 2.

1.7 Soft Matter Models for Biological Systems

Theoretical models based on soft matter physics have been previously employed to investigate a wide range of biological systems. A computationally implemented mathematical model based on the Landau-de Gennes theory for cholesteric LCs has been employed to investigate the effect of constraining surfaces on the development of helicoidal texture in biological fibrous composite [48,49]. These computations elucidated the need for a constraining surface that can direct the chiral self-assembly in a direction normal to it, to form a defect-free (monodomain) twisted plywood structure. An integrated flexoelectric/viscoelastic model for linear oscillatory dynamics of flexoelectric membranes embedded in viscoelastic media of relevance to outer

hair cells located in the inner ear has been developed based on the theory of nematic flexoelectricity in LC phases [50]. A continuum model based on Frank-Oseen formalism of LC phases has been developed to investigate the self-assembly mechanisms forming helicoidal textures and hexagonal fiber bundles in *in vitro* self-assembly of F-actin fibers [32]. Recently, theoretical work developed to predict the influence of anchoring energy of LCs on the orientation of the interfacial tension [51] has been proven to demonstrate the formation of complex surface features such as unduloids and helices experimentally observed in 3D viral structures arising through self-assembly [52]. Periodic relief arising at the free surface of a helicoidal plywood in some flowers' petals, and beetle exocuticle surfaces that play a key role in the iridescence of these structures, have been simulated using a mathematical model based on chiral self-assembly with air-surface interface driven by chiral capillarity [53]. This review article emphasizes the capability of theory and simulations based on anisotropic soft matter models [54–58] to yield testable and verifiable predictions of textural and rheological phenomena observed in real plant cell walls, in an attempt to verify the LC self-assembly model for plant cell wall synthesis and highlight the versatility of these models to simulate other biological/biomimetic systems. For an extensive review on mesoscopic models employed to quantitatively describe the structures and processes in biological systems, refer to [31,59].

The organization of this review article is as follows: Section 2 presents the model for chiral self-assembly driven by entropic and chiral interactions resulting in helicoidal plywood architecture. The model is validated by simulation of observed defects and textures in plant cell wall; in Section 3, curvature-induced planar self-assembly mechanism in plant cell walls is presented. A continuum model for this external field induced fiber ordering is presented and validated; Section 4 presents the application of these systems to other biological/biomimetic systems, highlighting the functionality that arises from the structures found in some plant cell walls; Section 5 presents the conclusion of this review on modeling self-assembly mechanisms in biological fibrous composites.

2 MODEL FOR HELICOIDAL PLYWOOD IN BIOLOGICAL FIBROUS COMPOSITES

The objective of this section is to demonstrate the role of LC self-assembly in the formation of helicoidal plywood architecture in plant cell wall and other biological LC analogues using mathematical models based on well-established liquid crystal theory.

The helicoidal plywood structure has the chiral order of a chiral-nematic liquid crystal, which possesses orientational order with a superposed rotation and layer periodicity [21,60]. Every elongated macromolecule or filament with a high aspect ratio, stably dispersed in a solvent, aligns spontaneously above a critical volume fraction, known as the Onsager critical limit [30]. This morphogenesis process, which leads to these intricate and fascinating structures, is thought to have the characteristics of a solid and a fluid state, enough fluidity for a structure to self-assemble and enough solidity to maintain the load-bearing capacity of the structure. In thermodynamic terms, self-assembly is a free energy minimization process driven by entropy. The excess Helmoltz free energy ΔF for the dispersion of microfibrils contains two competing entropic terms [47]:

$$\frac{\Delta F(\rho)}{k_B T} = \int f(\mathbf{u}_1) \ln(4\pi\rho f(\mathbf{u}_1)) d\mathbf{u}_1$$

$$- \frac{\rho}{2} \int f(\mathbf{u}_1) f(\mathbf{u}_2) \beta_1(\mathbf{u}_1, \mathbf{u}_2) d\mathbf{u}_1 d\mathbf{u}_2, \quad (2)$$

where $f(u)$ is the orientation distribution function, ρ is the number density of microfibrils, $\beta_1(\mathbf{u}_1, \mathbf{u}_2)$ is the excluded volume by a microfibril of orientation u_1 on a microfibril of orientation u_2. The first term corresponds to the entropy of mixing and favors random orientation of the microfibrils. The second term corresponds to exclude volume entropy, which increases with a decrease in the average angle between neighboring microfibrils. The inherent chirality of the molecules that build these materials results in a chiral microstructural organization. In addition to chiral interactions, other factors that influence the formation of liquid crystalline phase include: the shape anisotropy of the fibers, the ionic environment that regulates the charges on the fibers, the concentration of the fibers that drive the minimization of excluded volume and the type of LC organization in either single and/or biphasic states. According to the Onsager theory, this concentration-driven LC order appears in solutions of rods when the shape anisotropy (L_{eff}/D_{eff}) times the volume fraction (ϕ), i.e., $\phi L_{eff}/D_{eff}$, exceeds a critical value (usually close to 4) at which excluded volume is minimized [61]. For semi-flexible biopolymer chains, like cellulose fibrils, L_{eff} is the persistence length of the polymer chain and D_{eff} is effective diameter that takes into account deviations from uncharged rigid-rods (due to dispersion forces, hydration interactions, and surface charges) [30]. The persistence length of cellulose chains obtained from various cellulose-solvent systems *in vitro* has been reported in the range of 11–25 nm [62]. It is erroneous to arrive at a conclusion that there is not enough

material to form a LC phase during development of helicoidal plywoods in plant cell walls solely based on this calculation for the following reasons: (a) these calculations use absolute diameter instead of D_{eff} of the CMFs, due to the lack of *in vivo* experiments in plant cell wall; (b) it has been frequently observed that the isotropic–anisotropic transition predicted by the Onsager theory may be an order-of-magnitude larger than that observed experimentally, perhaps due to other factors such as molecular interactions. Ideal helicoidal plywood architecture directed from a constraining surface forms a defect-free monodomain with a constant helical pitch as depicted in Figures 4 and 5.

However, the extracellular domain of a plant cell in which this chiral self-assembly takes place is rich in secondary inclusions such as pit canals and other plant cells themselves. The inclusion of these secondary phases induces confinement of the LC material between them, and the resulting frustration in the mesophase is relieved through nucleation of defects and distortion of the pitch of the mesophase as shown in Figure 6. There is strong evidence that the solid helicoidal plywood architecture is formed through LC self-assembly by the existence of specific defect patterns observed in the presence of these secondary phases in the domain of self-assembly [63].

Defects in cholesteric phases include disclinations and dislocations due to the fact that at short length scales the material has orientational order but at long length scales it is layered as in a 1D solid. Disclinations involve distortion in the orientation of the cholesteric layers and can have singular (τ lines) or non-singular (λ lines) cores; in the former

the molecular order deviates from its homogeneous value, while in the latter it does not. The coreless non-singular disclination lines of core size of the order of p_0 have lower energy than the singular τ disclination lines of core size of the order of nanometers. Disclinations are characterized by a sign (sense of rotation) and strength (amount of rotation). Charge of an individual disclination can be $\pm 1/2$ or ± 1 and describes the amount and the sense of director rotation when encircling the defect core. The dislocations involve changes in the number of layers. The dislocation core can be compact non-split core or split into a pair of disclinations. Figure 7 shows an example of a disclination line of type λ^{+1} in the root nodule of Vicia [24] and texture predictions of the Landau de Gennes model, showing the presence of nonsingular λ^{+1} lines in a helicoidal polydomain texture that also includes singular $\tau^{-1/2}$ lines [49].

Apart from this correspondence in structure and defect textures between helicoidal cell walls and cholesteric mesophases, plant cell walls also exhibit arc patterns that deviate from ideal, monotonic helicoidal plywood depicted in Figure 1–5(a). Given the multifunctionality embedded in the PCW and different formation conditions more complex helicoids are found, including (i) doubly periodic structures, (ii) gradient pitch, (iii) discrete plywoods, and (iv) localized chiral pulses, shown in Figure 8. The fiber orientation in the doubly periodic plywoods has a large-scale periodicity which is a function of the two pitches present, $\mathbf{n}(z) = \mathbf{n}(z + m_1 p_{o1} + m_2 p_{o2})$, where m_i is the number of pitches in the layers of pitch p_{oi}. Since the pitch is a function of fiber concentration and solutes, couplings between LC order and solute
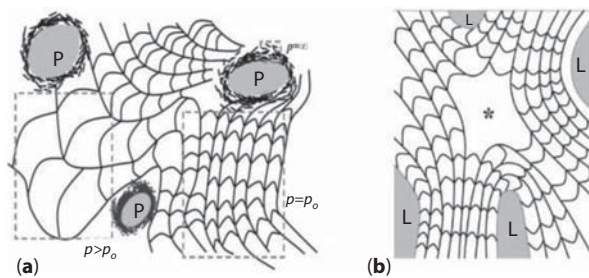
Figure 6 Helicoidal plywoods in plant cell walls with secondary phases. (a) Adaptation of helicoidal plywood to embedded pit canals (P inside the gray circles) by dilation of layers (shown by width changes in arc patterns) and bending of layers (bending of arced patterns) [24]; (b) A –1 saddle defect (denoted by *) in a natural helicoidal plywood due to inclusion of four (L) lumens in walnut [64] (Adapted from ref. [31]). For filled LCs, a defect of strength –(N–2)/2 is expected [41]. For the four (L) lumens, N=4 and the plywood has a –1 saddle defect (*).
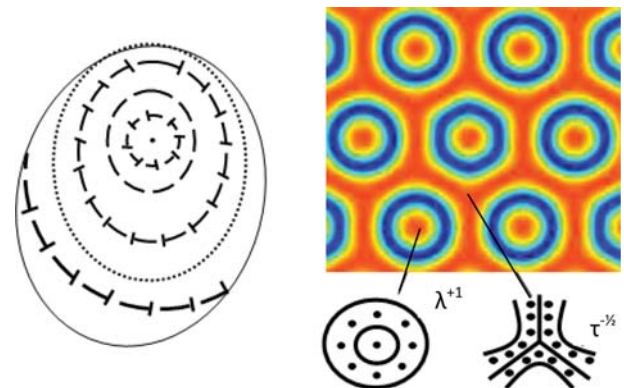
Figure 7 Fingerprinting chiral self-assembly in root nodule of *Vicia*. (a) λ^{+1} disclination in cross-section, in a twisted body of a root nodule of *Vicia* (Adapted from ref. [80]), (b) λ^{+1} and $\tau^{-1/2}$ disclination simulated using Landau de Gennes model [49,55].
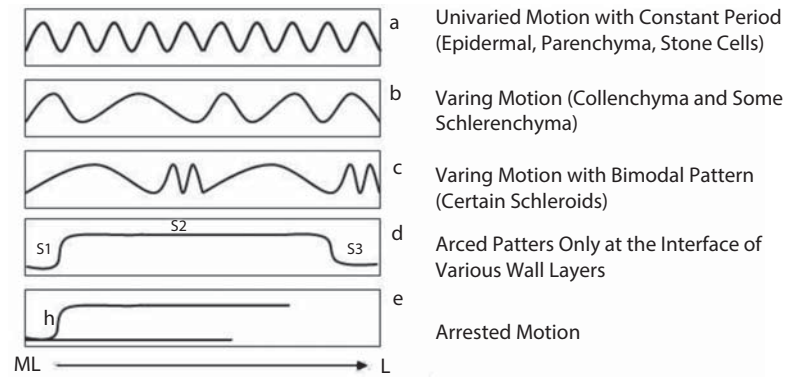
Figure 8 Various helicoidal wall expressions: **(a)** monotonic helicoid, **(b)** random pitched helicoid, **(c)** bimodal helicoid, **(d)** interlayer helicoid, **(e)** discontinued helicoid, ML – Middle lamella, L – Cell lumen. (Adapted from ref.[55])

concentration can give rise to doubly-periodic and gradient pitch structures. Discrete pitches involve finite rotations between neighboring layers, a fact observed in cholesteric DNA. Localized pulses describe a cholesteric layer immersed in a nematic matrix, a structure predicted for nematic polymers under flow. The variability of plywood structures is an indication of adaptability to changing chemo-mechanical environments and required multifunctionality [10].

The model for chiral self-assembly for PCW based on the Landau-de Gennes (LdG) theory expresses the free energy density of the solution of CMFs in terms of homogeneous and gradient elastic contributions. The short-range (long-range) effects are represented by a power series of tensor parameter order $\mathbf{Q}$ that quantifies the alignment of CMFs (gradient of tensor order parameter $\nabla\mathbf{Q}$). In the absence of an external field, the total free energy density of the mesophase (f) can be given in the following dimensionless form [48,59]:

$$f = f_{iso} + f_{sr} + f_{lr} \qquad (3(a))$$

$$f_{sr} = \left\{ \frac{1}{2}\left(1 - \frac{U}{3}\right)\mathrm{tr}\mathbf{Q}^2 - \frac{U}{3}\mathrm{tr}\mathbf{Q}^3 + \frac{U}{4}\left(\mathrm{tr}\mathbf{Q}^2\right)^2 \right\}, \quad (3(b))$$

$$f_{lr} = \frac{1}{2}\left\{ \left[\left(\frac{\xi}{h_0}\right)(\nabla\times\mathbf{Q}) + 4\pi\left(\frac{\xi}{p_0}\right)\mathbf{Q}\right]^2 + \upsilon\left[\left(\frac{\xi}{h_0}\right)(\nabla.\mathbf{Q})\right] \right\}$$
$$(3(c))$$

where f_{iso} is the free energy density of the isotropic (unordered) state, which depends on conventional thermodynamic parameters such as temperature, pressure, and concentration; f_{sr} and f_{lr} are, respectively, the short- and long-range contributions to the total free energy density f. The dimensionless parameter U is proportional to the dimensionless concentration

of anisotropic molecules, which drives the isotropic-chiral-nematic phase transition; U is related to the concentration C by the relation U = 3C/C*, where C* is the concentration of the CMFs at the phase transition from unordered-order state. The parameter ξ is a coherence/internal length that gives the distance over which variations of long-range orientational order can occur. This length represents the order of magnitude for the size of the core of a disclination defect. The parameter h_0 is a macroscopic length scale external/geometric length that gives the size of the domain. The parameter p_0 is the pitch of the chiral-nematic liquid-crystalline material. It is essential to recognize that this model is therefore of a mesoscopic nature since it includes a molecular length scale (ξ) and a macroscopic (h_0) length scale. The remaining parameter υ represents a measure of the elastic anisotropy of the material. The nematodynamics equation used to describe the time evolution of the tensor order parameter $\mathbf{Q}$ is given by:

$$-\gamma\frac{\partial\mathbf{Q}}{\partial t} = \frac{\delta f}{\delta\mathbf{Q}} = \left[\frac{\delta f}{\delta\mathbf{Q}} - \nabla.\frac{\delta f}{\delta\nabla\mathbf{Q}}\right] \qquad (4)$$

where the superscript [s] denotes symmetric and traceless tensors, and where γ is a rotational viscosity [48]. Substituting Eqn. 3 into Eqn. 4 yields the equation for spatio-temporal evolution of tensor order parameter $\mathbf{Q}(\mathbf{x},t)$. The objective of this section is to characterize the defect texturing mechanism as a function of chirality (p_0), elastic anisotropy (υ) and particle configuration. Figure 9 presents the alignment of CMFs computed using Eqn. 4 in a two-dimensional domain with a network of inclusions that forms a square (N=4), to replicate the cell lumen arrangement seen in Figure 6(b). The model (Eqns. 3,4) is able to reproduce the experimentally observed saddle defect observed in secondary cell wall of walnut [64]. The
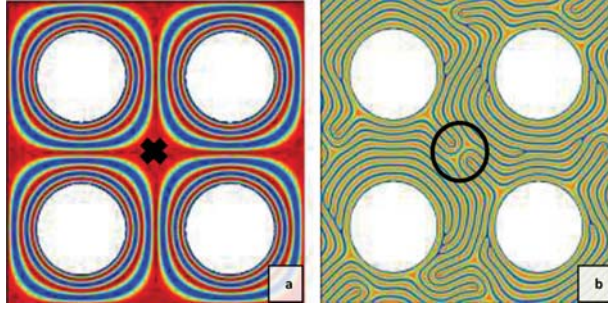
Figure 9 Surface plots of the CMF alignment observed in chiral LC phases at high elastic anisotropy. The fields change from blue to red as the CMF alignment changes from in-plane of the figure to perpendicular to the figure. **(a)** Tetragonal 2D blue phase at high elastic anisotropy υ=21, ξ/p_0=0.0125, N=4 (intermediate) [54]. The **x** mark indicates λ^{-1} disclination seen in Figure 6(b); **(b)** Cholesteric fingerprint texture at high elastic anisotropy υ=21, ξ/p_0=0.05, N=4 (at steady state). The circled region encompasses Lehmann cluster, a quadrupolar defect interaction observed in *in vitro* DNA self-assembly [55]. (Adapted from ref.[55])

defect is characterized to be a non-singular λ^{-1} defect. The theory and simulations presented in this section indicate that the material property and length scales that result in this biological structure are: large elastic anisotropy, large number of pitches within the confined space, and high concentration of CMFs (corresponding parameters in Eqn. 3: υ = 21, U = 6, (ξ/p_0) = 0.05, (ξ/h_0) = 0.0025). When the concentration of the CMFs is less than the critical value for isotropic-anisotropic phase transition (U < 3), an alternative CMF aligning mechanism that uses the curvature of the embedded matrix to promote unidirectional CMF alignment modes such as line, helical and ring modes is presented in Section 3. In addition to narrowing the parametric space to biological-relevant values that lead to the saddle texture of a biological plywood, the transient directed chiral self-assembly simulations in the presence of curved second phases provide support to LC model that the origin of the frozenin architecture in Bouligand's plywood is the cholesteric mesophase [21]. As the texture in Figure 9(a) is allowed to relax, further fingerprint textures with dislocations/dislocations presented in Figure 9(b) arise. The observed defect textures have the following characteristics: (a) non-singular disclinations of strength +1 (λ^{+1}) that involve bending of layers are energetically costly and are avoided, and (b) the layers tend to avoid bending and are locally planarly aligned through: (i) the nucleation of defects closer to the particle surface and (ii) the nucleation of quadrupolar defects such as Lehmann clusters, that are known to arise also in *in vitro* DNA self-assembly

[36]. This result is in good agreement with helicoidal textures formed from cellulose microfibrils through self-assembly in the cell wall of a prune with a triangular network of pit canals (P) embedded in cholesteric mesophase [24] depicted in Figure 6(b). The observed textures also follow experimental observations in three helical biological polymeric mesophases (last column in Table 2), namely PBLG (a polypeptide), DNA (a polynucleotide) and xanthan (a polysaccharide) [36]. Despite their different chemical nature, the phases given by all these biopolymers are devoid of solitary $\tau^{-1/2}$ disclinations. If present at all, these singular disclinations are observed only as $\tau^{-1/2}\lambda^{+1/2}$ disclination pairs. The results of our simulations at high elastic anisotropy corresponding to LC phases of semi-flexible polymeric mesogens (Figure 9(b)) are perfectly and quantitatively consistent with this experimental observation. The predicted value of elastic anisotropy during the formation of helicoidal texture indicates high energy cost associated with bending/splaying fibers in the helicoidal structure compared to twisting the fibers in such a packing. This measured value of elastic anisotropy agrees well with experimental measurements of elastic constants in biopolymeric mesophase of PBLG (*in vitro*) [65] and is further supported by bending and twisting costs estimated based on a continuum model for hexogonally packed chiral filament assemblies based on the Frank-Oseen formalism of LCs [66]. The defect textures predicted by the model obeys Zummer's rule that relates the net topological charge in a LC system with N secondary inclusions: $-(N-2)/2 = -1$ as observed in natural [54,55] and synthetic filled LCs [67].

The present model can be extended to explore other biologically relevant features of plywoods such as surface melting [21]. Figure 10 depicts the defect-generation during growth that occurs under surface melting. A layer of random fiber organization next to the substrate heals into a layered helicoid that then grows into defect-free monodomain plywood. Figure 10(a) shows the vertical growth from a disorded layer (random horizontal fiber row) predicted by the Landau-de Gennes model [49] and Figure 10(b) the corresponding biological texture of the elongating zone of the mung bean (*Vigna radiata*) seedling exhibiting similar features [68].

Thus, in addition to providing information on material properties and length scales that cannot be experimentally measured *in vivo*, the simulated transient defect pattern acts as a fingerprint for the formation of helicoidal plywoods in biological fibrous composites through directed chiral self-assembly under confinement.
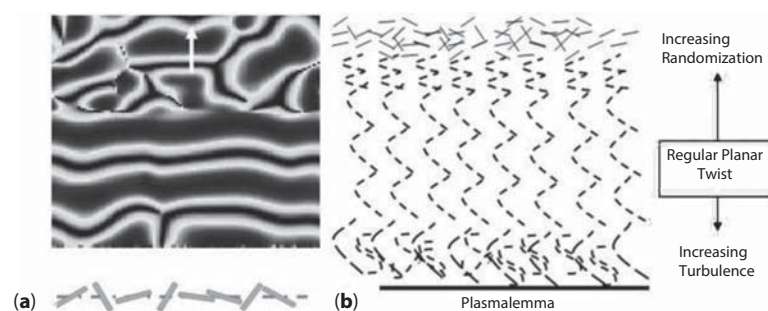
Figure 10 Fingerprinting chiral self-assembly in mung bean. (a) Simulated self-assembly under random ordering, leading to a helicoidal structure after a healing length of the order of the pitch (Adapted from G. de Luca and A. Rey, 2003), (b) Biological plywood of the elongating zone of the mung bean (Vigna radiata) seedling exhibiting similar features. (Adapted from ref. [68])

3 MODEL FOR UNIAXIAL FIBER ALIGNMENT IN BIOLOGICAL FIBROUS COMPOSITES

At concentrations below Onsager's critical limit (C < C*), excluded volume interactions and chiral interactions between the CMFs become less significant. Under these dilute conditions, helicoidal plywoods are not formed and CMF alignment has to be imparted through interaction of CMFs with an external field. Plant cell walls are cylindrical fiber-reinforced composites with circular (constant curvature around the membrane's circumference) or super-elliptical cross section (spatially varying curvature around the membrane's circumference) [69]. In this section, continuum models for curvature-induced planar self-assembly in fiber-laden membrane are used to demonstrate the possibility of unidirectional CMF alignment such as line, ring and helical modes (see Figure 3) arising through the delicate interplay between membrane geometry and embedded fiber order in biological fibrous composites with dilute fiber concentration. An example of the possible effect of membrane curvature on microfibril orientation in plant cell walls is found in the abrupt changes in microfibril angle in the S2 and S3 layers at the corners of juniper tracheid plant cells [18]. The existence of membrane curvature-fiber orientation coupling is further supported by the transient nature of helicoidal pattern in primary plant cell walls of mung bean, owing to the drastic change in cell curvature during simultaneous growth and deposition of primary cell wall [70]. Similar interactions between membrane surface geometry and filamentous macromolecules have been investigated in membrane curving proteins-lipid bilayer [71,72] and antimicrobial peptides-bacteria systems [73]. In an earlier attempt to estimate the influence of membrane curvature on
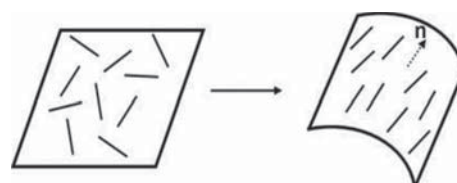
Figure 11 Schematic of curvature-induced 2D nematic LC self-assembly on membranes. At dilute CMF concentrations below Onsager's critical limit, the isotropic state observed on a flat membrane (left) may lead to a nematic state (right) due to curvature-mediated interactions.

embedded fibers, a theoretical model based on continuum elasticity theory for anisotropic membrane inclusions in lipid membranes was developed [74].

In the study of LCs, this alignment of molecules induced by an external field such as surface (bounding surface) curvature is called "paranematic ordering" and the free energy minimization process that drives the alignment of molecules on a 2D surface is called "planar self-assembly." The schematic of the proposed curvature-driven planar self-assembly model is presented in Figure 11. Cell walls with unidirectional CMF alignment can be considered as a two-dimensional fiber-reinforced membrane. Planar self-assembly mechanisms in these materials remain partially understood despite their biological and biomimetic relevance. An integrated mechanical model for curvature-driven planar self-assembly of rigid rods on an arbitrarily curved fluid membrane through novel surface phenomena such as curvophobic and curvophilic effects, by extending the Helfrich elastic theory of curved isotropic membranes to anisotropic curved membrane, has been applied to predict the uniaxial modes in plant cell walls [56–58]. Curvophilic (curvophobic) effects seek to align the CMFs along high (zero) curvature directions [56].

In biological fiber-laden membranes, curvophobic interactions may arise as an attempt to minimize the non-attachment penalty, the elastic energy cost associated with the rigid fibers not completely supported by the membrane when they are aligned in the direction of maximum curvature. On the other hand, curvophobic interactions may originate from any of the following mechanisms: (i) the fibers exhibiting preferential orientation over corrugated grooves on the membrane surface, known as Berreman anchoring [75], (ii) intrinsic nanoscale coiling of biological fibers predominantly modeled by the Helfrich elastic chiral filament model or Kirchhoff elastic theory of rods [76], (iii) membrane curvature induced by soft-mode instability of membranes caused due to the adsorbed fibers [77].

The total free energy of the fiber-laden membrane system per unit area $\hat{F}$ is posited to be [56–58]:

$$\hat{F} = \hat{F}_{membrane}(\mathbf{b}) + \hat{F}_{fiber}(\mathbf{S}) + \hat{F}_{coupling}(\mathbf{b} \cdot \mathbf{S}) \qquad (5)$$

where $\mathbf{b}$ is the tensor that quantifies the ambient curvature of the membrane and $\mathbf{S}$ is the fiber order parameter in 2D. When the free energy of the ensemble is minimized, the equilibrium fiber alignment and order are obtained as a function of dimensionless radius of the membrane [58]. Figure 12 depicts the fiber orientation modes in terms of cosine of equilibrium fiber orientation angle with respect to azimuthal coordinate ($\cos \alpha$) and equilibrium fiber order in terms of scalar order parameter (S), obtained by minimizing Eqn. 5 with typical parameters. At low dimensionless membrane radius, for $0 < R^* < 0.1847$, the curvophilic free energy is negligible and the curvophobic free energy is minimized, thus the fibers are aligned in the axial direction resulting in the line mode. At intermediate membrane radius, for $0.1847 < R^* < 0.3867$, the competition between the fiber interactions and curvophilic free energy aligns the fibers at an angle between 0–90°, resulting in the helical mode. At high membrane radius, for $R^* > 0.3867$, the curvophobic free energy is negligible and the curvophilic free energy is minimized, thus the fibers are aligned in the azimuthal direction resulting in the ring mode. At low membrane radius, the fibers are more uniformly aligned in the axial direction. As the membrane radius increases, the fiber order S decreases until a local minimum (cusp) is reached, due to the cancellation of free energy contributions from curvophobic and curvophilic interactions. At the onset of the ring mode, the fiber order S starts increasing until a local maximum is reached promoted by curvophilic interactions. At high membrane radii, the fiber order vanishes asymptotically as the membrane curvature vanishes, resulting in random fiber orientation.
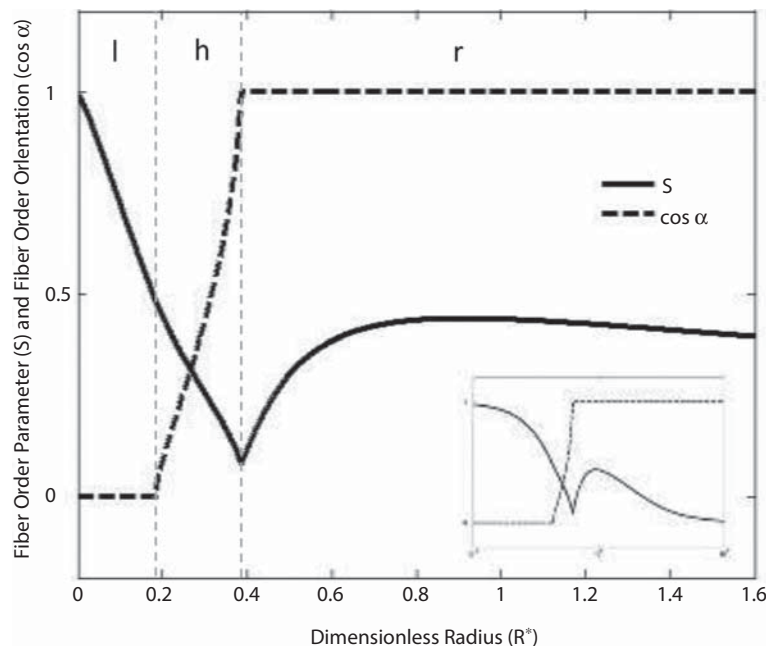

Figure 12 Fiber structure plot for cylindrical membranes of circular cross-section [58]. The three possible modes are: l – line mode, h – helical mode, r – ring mode. The order parameter displays a typical V shape and the orientation a step-like response as the radius increases. The inset semi-log plot shows fiber order vanishing asymptotically as $R^* \to \infty$.

Although the present model does not take into account temporal variation of cellulose microfibril concentration during different stages of cell wall deposition, the predicted fiber orientation (see Figure 12) is in good qualitative agreement with the experimental observations for the orientation of cellulose microfibrils in cell walls of trachieds of conifers based on field emission scanning microscopy [78]. The progressive changes in the orientation of cellulose microfibrils in primary and secondary layers of these plant cell walls are shown in Figure 13(a). A schematic of cell wall deposition process and corresponding changes in membrane shape are depicted in Figure 13(b). The initial layers of primary cell wall are deposited at the onset of cell growth when the membrane radius is small, resulting in line mode (Figure 13(a)-1, 13(b)-1). The final layers of primary cell wall are deposited towards the end of cell growth, when the membrane radius is large as the cell reaches its maximum size (Figure 13(b)-2). Consequently, the layers deposited in this phase exhibit ring mode (Figure 13(a)-2). This result is in agreement with experimental observations showing the orientation of microfibrils changing from line to ring mode in different plant species [78]. When the cell growth ceases the secondary cell wall layers are deposited from the inner side and the cell starts shrinking to become a lumen. As the radius of the membrane decreases due to the cell wall deposition, the fiber orientation changes to helical mode in the S_1 layer and the fiber angle with respect to azimuthal direction progressively changes

from 0–90° [78]. The S_2 layers deposited at further smaller membrane diameter exhibit further steeper fiber orientation closer to the line mode and show high fiber order (Figure 13(a)-3, 13(b)-3). The discrepancy between the experimentally observed helical or crossed helical modes and the model-based prediction of line mode in S_3 layer might be attributed to lignification of the S_3 layers before completion of cellulose microfibril alignment, as S_3 is the innermost layer deposited towards the end of the cell wall deposition process. This reasoning is further supported by wide variations in observed microfibril orientation in the innermost layers of S_3 among different tree species [78]. The model when solved on a membrane of spatially varying curvature, results in membrane with spatially graded fiber orientation and order [58]. This numerical prediction is consistent with an abrupt change in fiber angle in S_2 and S_3 at the corners reported in plant cell walls of juniper tracheid. The fiber orientation angle in the corners measured with respect to azimuthal coordinate (α) is 15 to 25° greater than in the sides [18].

This novel coupling between in-plane fiber orientation and fiber order and the curvature of the membranes demonstrated by plant cell walls in nature has the potential to open up a novel venue to control two-dimensional anisotropic soft matter with tailored functionalities [79]. To understand the dynamic coupling between embedded fibers and membrane curvature and its role in dynamic reorientation of CMFs during plant cell growth, refer to [57].
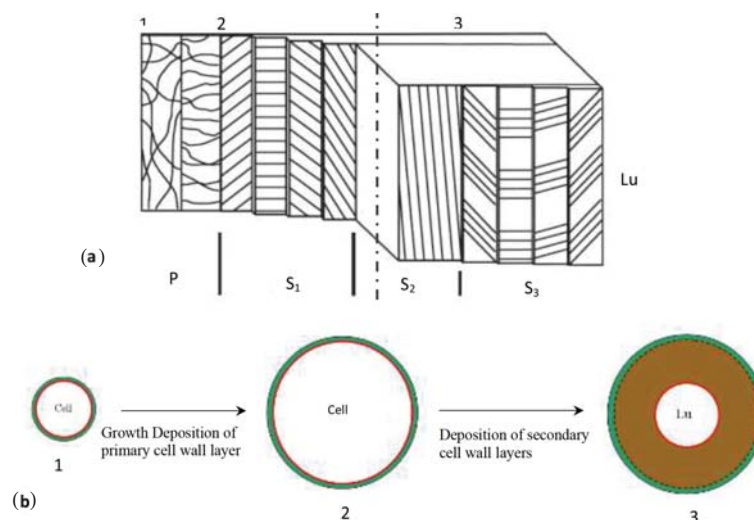
Figure 13 Cellulose microfibril orientation in some plant cell walls and their deposition process. **(a)** A model for the orientation of cellulose microfibrils viewed from the lumen side in the cell walls of tracheids of conifers: P – Primary cell wall, S_1, S_2, S_3 – Secondary cell wall layers 1, 2, 3, Lu – Lumen. (Adapted from ref. [78]) **(b)** A schematic of cell wall deposition process and corresponding changes in membrane shape: Lu – Lumen. The changes in curvature correspond to different fiber orientation and order, as per Figure 11.

4 APPLICATION OF PCW-BASED ANISOTROPIC SOFT MATTER MODELS

Besides facilitating access to length and times scales, material properties, processing conditions and interactions that cannot be easily determined experimentally if at all, the anisotropic cell wall models reviewed in this article can be employed to investigate material processing and defect texture formation in other biological and biomimetic systems. Figure 14 illustrates some of the biomimetic applications of helicoidal plywoods demonstrating various functionalities.

Material processing: Spiral and double spiral defect structures observed in helicoidal plywoods of crab (*Carcinus maenas L*) composed of chitin fibrils in the presence and absence of a vertical canal (biological LC analogue) [32], silk spinning of (*N. clavipes*) spiders *in vivo* (biological cholesteric mesophase) [40], defects arising during self-assembly of DNA, PBLG and Xanthan *in vitro* (biomimetic biopolymeric mesophases) [36] and chiral self-assembly in the presence of embedded polygonal particle networks arising in carbon-fiber-reinforced carbon composites [80], LC emulsions [81] and filled cholesterics [82] (biomimetic synthetic mesophases) can all be analyzed using the model for helicoids formation in PCW based on Landau de Genne's LC theory. Understanding the defect texturing mechanisms in cholesteric mesophase is crucial in developing potential applications such as supramolecular templating [83], spatial distribution control of nanoparticles [84] and biomimetic material processing [10]. The knowledge gained in this study is of significant importance for researchers in the fields of material science and tissue engineering trying to mimic the ultrastructure and mechanical properties of bone tissue using cellulosic material [85,86].

Advanced materials: Variable stiffness materials and structures are increasingly finding applications in several diverse fields such as next-generation automobiles, aerospace components, biomorphing structures, and sports equipments. Achieving this property through spatially varying fiber orientation in fibrous composite structures has been demonstrated [87]. Although at a different length scale, shape fluctuations arising due to elastic inhomogeneities induced by the graded fiber orientation [58] are known to induce local change in bending rigidity and spontaneous membrane curvature and play a crucial role in morphogenesis in biological systems such as pollen grains [88]. The planar self-assembly mechanism and the novel interactions reviewed in this article have the potential to inspire energy-efficient self-assembly mechanisms for synthesizing variable stiffness composites.

Optics: The twist of the helicoidal plywood structure introduces macroscopic chirality resulting in three important optical properties: pseudo-Bragg reflections, circular dichroism, and rotatory power [10]. Bragg reflections give rise to iridescent colors when subjecting the helix to white light; circular dichorism results in selective reflections such that at a particular wavelength incident right-handed circular polarized light is transmitted through a right-handed helix, but left-handed circular polarized light is reflected. Bragg reflection based on cholesteric order is the source of beetle's optical properties [89]. Plants have evolved mechanisms of light transmission and absorption for form, function, and growth; the role of helicoids on plant's optics is believed to play a role in the root's functionalities [90]. Helicoidal plywoods in plant cell walls also exhibit pitch gradients, double periodicities and chiral inversion (Figure 8). These observed plant-based chiral composites are expected to generate new optical capabilities [10].

Mass transfer systems: Chiral materials couple mass and heat transfer with orientation and flow kinematics, in which absorption and delivery of embedded solutes can be manipulated by changes in fiber orientation, serving as a new principle for drug delivery systems and gas sensors [10]. Recently polymerization in cholesteric LCs that leads to chiral polymer ribbons have been demonstrated [90]. Polymerization in chiral media extends the established route of chemical synthesis in structured media for supramolecular architectures with controlled chirality. Coupling mass transfer with the chiral self-assembly model can yield a robust tool to analyze these systems.

Model system for 2D anisotropic soft matter: The PCW can be considered a model system to study planar self-assembly mechanisms in other 2D anisotropic soft matters such as nematic shells (metamaterials) [91], graphite foam (heat transfer element) [92], membrane-peptide interaction (antibacterial peptides on bacterial cells, Alzheimer's amyloid beta peptide on cell plasma membranes) [93], LC films and interfaces [94], and
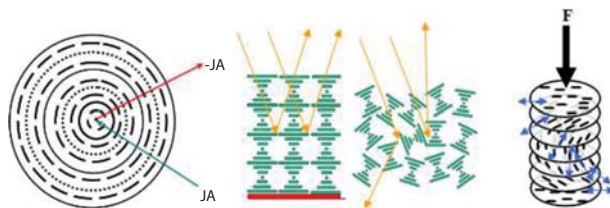
Figure 14 Biomimetic applications of helicoidal plywoods demonstrating various functionalities: (a) Mass transfer: Adsorption/delivery systems for drug delivery applications and gas sensors; (b) Optics (optical filters, lasers, chiral photonics); (3) Mechanical efficiency: Chiral graded fiber composites. (Adapted from ref. [10])

stress sensors [95–97] that find applications in industries, biomedical and biomimetic materials research.

5 CONCLUSIONS

Excellence in performance of natural materials arises from precise control over their structure at all length scales, accomplished through self-assembly processes employed in synthesizing these materials. Understanding the mechanisms underlying nature's material synthesis can inspire design and fabrication of efficient structural and functional materials. Theory and simulation can be used as pragmatic tools that may resolve time and length scales not easily accessible to experiments. The mathematical models reviewed in this paper elucidate the principles and mechanisms that govern the thermodynamics, material science, and elasticity of biological anisotropic soft matter that are involved in growth/self-assembly/material processing in multifunctional biological fibrous composites such as plant cell wall, insect exocuticle, and human compact bone.

ACKNOWLEDGEMENTS

REFERENCES

1. M. Meyers, A. Hodge, and R. Roeder, Biological materials science and engineering: Biological materials, biomaterials, and biomimetics. *JOM J Miner., Metals Mater. Soc.* **60**, 21 (2008).

2. E. Arzt, Biological and artificial attachment devices: Lessons for materials scientists from flies and geckos. *Mater. Sci. Eng. C*, **26**, 1245 (2006).

3. W.M. Kier, The musculature of squid arms and tentacles: Ultrastructural evidence for functional differences. *J. Morphol.* **185**, 223 (1985).

4. A.L. Holt, A.M. Sweeney, S. Johnsen, and D.E. Morse, A highly distributed Bragg stack with unique geometry provides effective camouflage for Loliginid squid eyes. *J. R. Soc. Interface* **8**, 1386 (2011).

5. S. Hunt and A. El Sherief, A periodic structure in the 'pen'chitin of the squid *Loligo vulgaris. Tissue Cell* **22**, 191 (1990).

6. A. Gautieri, S. Vesentini, A. Redaelli, and M.J. Buehler, Hierarchical structure and nanomechanics of collagen microfibrils from the atomistic scale up. *Nano Lett.* **11**, 757 (2011).

7. F.-C. Yang, R. Peters, H. Dies, and M.C. Rheinstadter, Hierarchical, self-similar structure in native squid pen. *Soft Matter* **10**, 5541 (2014).

8. Y. Bouligand, Twisted fibrous arrangements in biological materials and cholesteric mesophases. *Tissue Cell* **4**, 189 (1972).

9. D. Raabe, P. Romano, C. Sachs, H. Fabritius, A. Al-Sawalmih, S.-B. Yi, G. Servos, and H. Hartwig, Microstructure and crystallographic texture of the chitin–protein network in the biological composite material of the exoskeleton of the lobster *Homarus americanus. Mater. Sci. Eng. A* **421**, 143 (2006).

10. A.D. Rey, D. Pasini, and Y.K. Murugesan, Multiscale modeling of plant cell wall architecture and tissue mechanics for biomimetic applications, in *Biomimetics: Nature-Based Innovation*, Y. Bar-Cohen, (Ed.), pp. 131–168, CRC press (2011).

11. A.R. Studart, Towards high-performance bioinspired composites. *Adv. Mater.* **24**, 5024 (2012).

12. J. Jin, P. Hassanzadeh, G. Perotto, W. Sun, M.A. Brenckle, D. Kaplan, F.G. Omenetto, and M. Rolandi, A biomimetic composite from solution self-assembly of chitin nanofibers in a silk fibroin matrix. *Adv. Mater.* **25**, 4482 (2013).

13. P. Visakh and S. Thomas, Preparation of bionanomaterials and their polymer nanocomposites from waste and biomass. *Waste Biomass Valor.* **1**, 121 (2010).

14. D.J. Cosgrove and M.C. Jarvis, Comparative structure and biomechanics of plant primary and secondary cell walls. *Front. Plant Sci.* **3**, 204 (2012).

15. L. Dupuy, J. Mackenzie, and J. Haseloff, Coordination of plant cell division and expansion in a simple morphogenetic system. *Proc. Natl. Acad. Sci.* **107**, 2711 (2010).

16. C.T. Brett and J.R. Hillman, *Biochemistry of Plant Cell Walls*, CUP Archive, (1985).

17. L.J. Gibson, The hierarchical structure and mechanics of plant materials. *J. R. Soc. Interface* **9**, 2749 (2012).

18. S.A. Wainwright, *Mechanical Design in Organisms*, Princeton University Press (1982).

19. A.M.C. Emons and B.M. Mulder, How the deposition of cellulose microfibrils builds cell wall architecture. *Trends Plant Sci.* **5**, 35 (2000).

20. N. Gierlinger, S. Luss, C. König, J. Konnerth, M. Eder, and P. Fratzl, Cellulose microfibril orientation of Picea abies and its variability at the micron-level determined by Raman imaging. *J. Exp. Bot.* **61**, 587 (2010).

21. A.C. Neville, *Biology of Fibrous Composites: Development Beyond the Cell Membrane*, Cambridge University Press (1993).

22. B. Vian, J.-C. Roland, and D. Reis, Primary cell wall texture and its relation to surface expansion. *Int. J. Plant Sci.* **154**, 1 (1993).

23. M. Giraud-Guille, Twisted plywood architecture of collagen fibrils in human compact bone osteons. *Calcif. Tissue Int.* **42**, 167 (1988).

24. J. Roland, D. Reis, B. Vian, B. Satiat-Jeunemaitre, and M. Mosiniak, Morphogenesis of plant cell walls at the supramolecular level: Internal geometry and versatility of helicoidal expression. *Protoplasma* **140**, 75 (1987).

25. R.J. Cyr, Microtubules in plant morphogenesis: Role of the cortical array, *Annu. Rev. Cell Biol.* **10**, 153 (1994).

26. K. Sugimoto, R. Himmelspach, R.E. Williamson, and G.O. Wasteneys, Mutation or drug-dependent microtubule disruption causes radial swelling without altering

parallel cellulose microfibril deposition in Arabidopsis root cells. *Plant Cell Online* **15**, 1414 (2003).

27. A. Emons, J. Derksen, and M. Sassen, Do microtubules orient plant cell wall microfibrils? *Physiol. Plant.* **84**, 486 (1992).

28. S.C. Mueller and R.M. Brown Jr, The control of cellulose microfibril deposition in the cell wall of higher plants. *Planta* **154**, 501 (1982).

29. S.C. Cowin, Do liquid crystal-like flow processes occur in the supramolecular assembly of biological tissues? *J. Non-Newtonian Fluid Mech.* **119**, 155 (2004).

30. A.M. Donald, A.H. Windle, and S. Hanna, *Liquid Crystalline Polymers*, Cambridge University Press (2006).

31. A.D. Rey, Liquid crystal models of biological materials and processes. *Soft Matter* **6**, 3402 (2010).

32. G.M. Grason and R.F. Bruinsma, Chirality and equilibrium biopolymer bundles. *Phys. Rev. Lett.* **99**, 098101 (2007).

33. E.A. Zimmermann, B. Gludovatz, E. Schaible, N.K. Dave, W. Yang, M.A. Meyers, and R.O. Ritchie, Mechanical adaptability of the Bouligand-type structure in natural dermal armour. *Nat. Commun.* **4**, 2634 (2013).

34. R.O. Prum and R.H. Torres, Structural colouration of mammalian skin: Convergent evolution of coherently scattering dermal collagen arrays. *J. Exp. Biol.* **207**, 2157 (2004).

35. M.-M. Giraud-Guille, Twisted liquid crystalline supramolecular arrangements in morphogenesis. *Intern. Rev. Cytol.* **166**, 59 (1996).

36. F. Livolant and Y. Bouligand, Liquid crystalline phases given by helical biological polymers (DNA, PBLG and xanthan). Columnar textures. *J. Phys.* **47**, 1813 (1986).

37. F. Livolant and Y. Bouligand, New observations on the twisted arrangement of dinoflagellate chromosomes. *Chromosoma* **68**, 21 (1978).

38. D.P. Knight and D. Feng, Some observations on the collagen fibrils of the egg capsule of the dogfish *Scyliorhinus canicula*. *Tissue Cell* **26**, 385 (1994).

39. A. Neville and B. Luke, A biological system producing a self-assembling cholesteric protein liquid crystal. *J. Cell Sci.* **8**, 93 (1971).

40. F. Vollrath and D.P. Knight, Liquid crystalline spinning of spider silk. *Nature* **410**, 541 (2001).

41. M. Adams and S. Fraden, Phase behavior of mixtures of rods (tobacco mosaic virus) and spheres (polyethylene oxide, bovine serum albumin). *Biophys. J.* **74**, 669 (1998).

42. B. Kupchinov, S. Ermakov, V. Rodnenkov, S. Bobrysheva, E. Beloenko, and V. Kestelman, Role of liquid crystals in the lubrication of living joints. *Smart Mater. Struct.* **2**, 7 (1993).

43. J.-F. Revol, H. Bradford, J. Giasson, R. Marchessault, and D. Gray, Helicoidal self-ordering of cellulose microfibrils in aqueous suspension. *Int. J. Biol. Macromol.* **14**, 170 (1992).

44. G.M. Clore, M.R. Starich, and A.M. Gronenborn, Measurement of residual dipolar couplings of macromolecules aligned in the nematic phase of a colloidal suspension of rod-shaped viruses. *J. Am. Chem. Soc.* **120**, 10571 (1998).

45. E. Barry, Z. Hensel, Z. Dogic, M. Shribak, and R. Oldenbourg, Entropy-driven formation of a chiral liquid-crystalline phase of helical filaments. *Phys. Rev. Lett.* **96**, 018305 (2006).

46. J.M. Davies and C. Viney, Water–mucin phases: Conditions for mucus liquid crystallinity. *Thermochim. Acta* **315**, 39 (1998).

47. E. Belamie, G. Mosser, F. Gobeaux, and M.-M. Giraud-Guille, Possible transient liquid crystal phase during the laying out of connective tissues: -chitin and collagen as models. *J. Phys. Condens. Matter* **18**, S115 (2006).

48. G. De Luca and A. Rey, Monodomain and polydomain helicoids in chiral liquid-crystalline phases and their biological analogues. *Eur. Phys. J. E Soft Matter Biol. Phys.* **12**, 291 (2003).

49. G. De Luca and A.D. Rey, Chiral front propagation in liquid-crystalline materials: Formation of the planar monodomain twisted plywood architecture of biological fibrous composites. *Phys. Rev. E* **69**, 011706 (2004).

50. M. Abou-Dakka, E. Herrera-Valencia, and A.D. Rey, Linear oscillatory dynamics of flexoelectric membranes embedded in viscoelastic media with applications to outer hair cells. *J. Non-Newtonian Fluid Mech.* **185**, 1 (2012).

51. A.-G. Cheong and A.D. Rey, Cahn–Hoffman capillarity vector thermodynamics for curved liquid crystal interfaces with applications to fiber instabilities. *J. Chem. Phys.* **117**, 5062 (2002).

52. S. Oh, E.A. Kwak, S. Jeon, S. Ahn, J.M. Kim, and J. Jaworski, Responsive 3D microstructures from virus building blocks. *Adv. Mater.* **26**, 5217 (2014).

53. P. Rofouie, D. Pasini, and A.D. Rey, Nanostructured free surfaces in plant-based plywoods driven by chiral capillarity. *Colloids Interface Sci. Commun.* **1**, 23 (2014).

54. Y.K. Murugesan and A.D. Rey, Modeling textural processes during self-assembly of plant-based chiral-nematic liquid crystals. *Polymers* **2**, 766 (2010).

55. Y.K. Murugesan, D. Pasini, and A.D. Rey, Defect textures in polygonal arrangements of cylindrical inclusions in cholesteric liquid crystal matrices. *Soft Matter* **9**, 1054 (2013).

56. A.D. Rey and Y.K. Murugesan, Mechanical model for fiber-laden membranes. *Continuum Mech. Thermodyn.* **23**, 45 (2011).

57. Y.K. Murugesan and A.D. Rey, Structure and rheology of fiber-laden membranes via integration of nematodynamics and membranodynamics. *J. Non-Newtonian Fluid Mech.* **165**, 32 (2010).

58. Y.K. Murugesan, D. Pasini, and A.D. Rey, Microfibril organization modes in plant cell walls of variable curvature: A model system for two dimensional anisotropic soft matter. *Soft Matter* **7**, 7078 (2011).

59. A.D. Rey, E. Herrera-Valencia, and Y.K. Murugesan, Structure and dynamics of biological liquid crystals. *Liq. Cryst.* **41**, 430 (2014).

60. P.-G. De Gennes and J. Prost, *The Physics of Liquid Crystals*, Clarendon press, Oxford (1993).

61. L. Onsager, The effects of shape on the interaction of colloidal particles. *Ann. N. Y. Acad. Sci.* **51**, 627 (1949).

62. L.M. Kroon-Batenburg, P.H. Kruiskamp, J.F. Vliegenthart, and J. Kroon, Estimation of the persistence length of polymers by MD simulations on small fragments in solution. Application to cellulose. *J. Phys. Chem. B* **101**, 8454 (1997).

63. D. Reis, J. Roland, M. Mosiniak, D. Darzens, and B. Vian, The sustained and warped helicoidal pattern of a xylan-cellulose composite: The stony endocarp model. *Protoplasma* **166**, 21 (1992).

64. D. Reis, J. Roland, M. Mosiniak, D. Darzens, and B. Vian, The sustained and warped helicoidal pattern of a xylan-cellulose composite: The stony endocarp model. *Protoplasma* **166**, 21 (1992).

65. R.B. Meyer, F. Lonberg, V. Taratuta, S. Fraden, S.-D. Lee, and A.J. Hurd, Measurements of the anisotropic viscous and elastic properties of lyotropic polymer nematics. *Faraday Discuss. Chem. Soc.* **79**, 125 (1985).

66. G.M. Grason, Braided bundles and compact coils: The structure and thermodynamics of hexagonally packed chiral filament assemblies. *Phys. Rev. E* **79**, 041919 (2009).

67. G. Gupta and A.D. Rey, Texture rules for concentrated filled nematics. *Phys. Rev. Lett.* **95**, 127802 (2005).

68. J.-C. Roland, D. Reis, and B. Vian, Liquid crystal order and turbulence in the planar twist of the growing plant cell walls. *Tissue Cell*, **24**, 335 (1992).

69. I. Burgert, M. Eder, N. Gierlinger, and P. Fratzl, Tensile and compressive stresses in tracheids are induced by swelling based on geometrical constraints of the wood cell. *Planta* **226**, 981 (2007).

70. J.-C. Roland, D. Reis, M. Mosiniak, and B. Vian, Cell wall texture along the growth gradient of the mung bean hypocotyl: Ordered assembly and dissipative processes. *J. Cell Sci.* **56**, 303 (1982).

71. M. Simunovic, A. Srivastava, and G.A. Voth, Linear aggregation of proteins on the membrane as a prelude to membrane remodeling. *Proc. Natl. Acad. Sci.* **110**, 20396 (2013).

72. J. Zimmerberg and M.M. Kozlov, How proteins produce cellular membrane curvature. *Nat. Rev. Mol. Cell Biol.* **7**, 9 (2005).

73. M. Tang and M. Hong, Structure and mechanism of β-hairpin antimicrobial peptides in lipid bilayers from solid-state NMR spectroscopy. *Mol. BioSyst.* **5**, 317 (2009).

74. M. Fošnaric, K. Bohinc, D.R. Gauger, A. Iglic, V. Kralj-Iglic, and S. May, The influence of anisotropic membrane inclusions on curvature elastic properties of lipid membranes. *J. Chem. Inf. Model.* **45**, 1652 (2005).

75. J.-B. Fournier and P. Galatola, Coarse-graining analysis of the Berreman anchoring *Phys. Rev. E* **60**, 2404 (1999).

76. Q. Liu, Y. Liu, B. Hu, and Z. Ou-Yang, Fourth order elastic chiral filament model and the centerline of uniform Kirchhoff elastic rod. *Phys. Lett. A* **352**, 358 (2006).

77. D.-W. Lee, S.-K. Ihm, and K.-H. Lee, Synthesis of a mesoporous titania/silica and its application to a composite membrane with high hydrothermal stability. *Desalination* **199**, 363 (2006).

78. H. Abe and R. Funada, Review-the orientation of cellulose microfibrils in the cell walls of tracheids in conifers. A model based on observations by field emission-scanning electron microscopy. *IAWA Jl.(NS)* **26**, 161 (2005).

79. A.M. Turner, V. Vitelli, and D.R. Nelson, Vortices on curved surfaces. *Rev. Modern Phys.* **82**, 1301 (2010).

80. Y. Bouligand, Defects and textures in cholesteric analogues given by some biological systems. *J. Phys. Colloques* **36**, C1 (1975).

81. M. Yada, J. Yamamoto, and H. Yokoyama, Spontaneous formation of regular defect array in water-in-cholesteric liquid crystal emulsions. *Langmuir* **18**, 7436 (2002).

82. J. Lintuvuori, K. Stratford, M. Cates, and D. Marenduzzo, Colloids in cholesterics: Size-dependent defects and non-Stokesian microrheology. *Phys. Rev. Lett.* **105**, 178302 (2010).

83. K.E. Shopsowitz, W.Y. Hamad, and M.J. MacLachlan, Flexible and iridescent chiral nematic mesoporous organosilica films. *J. Am. Chem. Soc.* **134**, 867 (2012).

84. K. Higashiguchi, K. Yasui, M. Ozawa, K. Odoi, and H. Kikuchi, Spatial distribution control of polymer nanoparticles by liquid crystal disclinations. *Polym. J.* **44**, 632 (2012).

85. N. Nassif, F. Gobeaux, J. Seto, E. Belamie, P. Davidson, P. Panine, G. Mosser, P. Fratzl, and M.-M. Giraud Guille, Self-assembled collagen– apatite matrix with bone-like hierarchy. *Chem. Mater.* **22**, 3307 (2010).

86. M. Zaborowska, A. Bodin, H. Bäckdahl, J. Popp, A. Goldstein, and P. Gatenholm, Microporous bacterial cellulose as a potential scaffold for bone regeneration. *Acta Biomater.* **6**, 2540 (2010).

87. Z. Gurdal and R. Olmedo, In-plane response of laminates with spatially varying fiber orientations-Variable stiffness concept. *AIAA J.* **31**, 751 (1993).

88. E. Katifori, S. Alben, E. Cerda, D.R. Nelson, and J. Dumais, Foldable structures and the natural design of pollen grains. *Proc. Natl. Acad. Sci.* **107**, 7635 (2010).

89. V. Sharma, M. Crne, J.O. Park, and M. Srinivasarao, Structural origin of circularly polarized iridescence in jeweled beetles. *Science* **325**, 449 (2009).

90. M. Goh, S. Matsushita, and K. Akagi, From helical polyacetylene to helical graphite: Synthesis in the chiral nematic liquid crystal field and morphology-retaining carbonisation. *Chem. Soc. Rev.* **39**, 2466 (2010).

91. S. Kralj, R. Rosso, and E.G. Virga, Curvature control of valence on nematic shells. *Soft Matter* **7**, 670 (2011).

92. N.C. Gallego and J.W. Klett, Carbon foams for thermal management. *Carbon* **41**, 1461 (2003).

93. Y. Verdier and B. Penke, Binding sites of amyloid β-peptide in cell plasma membrane and implications for Alzheimer's disease. *Curr. Protein Pept. Sci.* **5**, 19 (2004).

94. P.S. Drzaic, Reorientation dynamics of polymer dispersed nematic liquid crystal films. *Liq. Cryst.* **3**, 1543 (1988).

95. S. Martellucci, A.N. Chester, and A.G. Mignani, *Optical Sensors and Microsystems.* New York, Boston, London (2002).

96. A.G. Kottapalli, M. Asadnia, J. Miao, G. Barbastathis, and M.S. Triantafyllou, A flexible liquid crystal polymer MEMS pressure sensor array for fish-like underwater sensing. *Smart Mater. Struct.* **21**, 115030 (2012).

97. A.D. Rey, P. Servio, and E. Herrera-Valencia, Bioinspired model of mechanical energy harvesting based on flexoelectric membranes. *Phys. Rev. E* **87**, 022505 (2013).